Interhemispheric Anti-Phase Variability in Mesospheric Climate Driven by Summer Polar Upwelling During Solstice Months

Liang Zhang¹, Zhongfang Liu¹, Brian Tinsley²

State Key Laboratory of Marine Geology, Tongji University, Shanghai, 200092, China Physics Department, University of Texas at Dallas, Richardson, Texas, 75080, USA

Correspondence to: Liang Zhang (Liangzhang420@tongji.edu.cn)

Abstract. The upper mesosphere, a transition region between Earth's atmosphere and space, is characterized by complex interactions among water vapor (H₂O), atomic hydrogen (H), ozone (O₃), atomic oxygen (O), and temperatures. Using MLS, SABER, and SOFIE satellite data, we explore the upwelling-driven interannual variability of temperatures near 90 km (T90) and atmospheric constituents during solstice months, revealing a bottom-up control mechanism of "upwelling—H₂O(H)—O₃(O)—T90" in the two hemispheres. First, summer polar upwelling transports H₂O upward, which is then transported toward the winter hemisphere by meridional winds. Subsequently, the hydration increases H via photolysis and depletes O₃ in the winter hemisphere through H-driven catalytic loss. The O varies in pace with O₃ due to chemical equilibrium, and the radiative and chemical heating by O/O₃ reactions reduces the T90 in the winter hemisphere (T90_w). Second, upwelling-induced cooling promotes polar mesospheric cloud (PMC) formation, with ice particle growth blocking H₂O transport and dehydrating heights above PMCs. This dehydration reduces H abundance, thereby decreasing H-driven O₃ loss. Meanwhile, the colder temperatures directly increase O₃ through ozone kinetics. The enhanced O₃, together with the coupled O, collectively increase the summer polar temperatures above 90 km (T90_s). This anti-phase interannual variability between hemispheres, mediated by PMC microphysics and H₂O-O₃ chemistry, establishes summer polar upwelling as a fundamental driver of mesospheric climate and highlights the importance of dynamical-chemical coupling in the upper mesosphere.

1 Introduction

The summer upper mesosphere is the coldest region on Earth's atmosphere, with temperatures as low as 130 K due to the adiabatic cooling of gravity wave-driven upwelling (Plane *et al.*, 2023). During solstice months, zonal winds are westward below ~90 km and eastward above, and meridional winds flow from summer to winter hemispheres (Ramesh *et al.*, 2024). Despite recent advances in mesospheric wind observations, direct measurements of vertical winds remain challenging (Lee *et al.*, 2024; Vincent *et al.*, 2019; Zhang *et al.*, 2020). The upper mesosphere exhibits complex couplings between dynamics and chemistry, particularly through H₂O and O₃ interactions that remain incompletely understood.

30 1.1 Water vapor and PMC dynamics

Upwelling and methane oxidation are primary H₂O sources in the upper mesosphere (Lübken et al., 2018; Shi et al., 2023). The rapid decrease of H₂O with altitude in the upper mesosphere (Figure 1a) is mainly caused by the photolysis of solar ultraviolet (UV) radiation, particularly in the summer polar region under continuous illumination. Fig. 1 demonstrates how summer polar upwelling creates concurrently temperature minima and H₂O maxima in the summer hemisphere. These conditions promote PMC formation between 80 km and 90 km (Rapp and Thomas, 2006), which subsequently redistributes H₂O through the well-established freeze-drying effect (Hervig et al., 2015; von Zahn and Berger, 2003). This top-down process, involving ice particle nucleation, growth, sedimentation, and sublimation, produces dehydration above PMCs and subsequently hydration below (Hultgren and Gumbel, 2014), with clear H₂O depletion visible above 60°S-80°S PMCs in Fig. 1a. Siskind et al. (2018) successfully simulated the dehydration and hydration above and below PMCs, which extend to midlatitudes due to meridional circulations (Fig. 1 therein). Current PMC models systematically overestimate the dehydration/hydration magnitudes (Bardeen et al., 2010; Lübken et al., 2009), suggesting an incomplete understanding of PMC formation. PMC variability is modulated by various dynamical processes, including gravity waves (Gao et al., 2018), planetary waves (Liu et al., 2015), tides (Fiedler and Baumgarten, 2018), and inter-hemispheric coupling (Gumbel and Karlsson, 2011). While solar UV theoretically influences H₂O and thus PMCs (Remsberg et al., 2018), the 11-year solar signal is insignificant over the past two decades (Hervig et al., 2019; Vellalassery et al., 2023), highlighting the need to identify alternative drivers.

1.2 Ozone chemistry and variability

In the upper mesosphere, the O concentrations increase sharply with altitude due to solar photolysis of O_2 (Mlynczak *et al.*, 2013), and the three-body recombination reaction of O produces a secondary ozone layer near 90 km (O+O₂+M \rightarrow O₃+M) (Smith *et al.*, 2013). The O exhibits a long photochemical lifetime near the mesopause (days to months), consequently, its daily and seasonal variability is governed by vertical transport processes, including tides and downwelling of the mean circulation (Smith *et al.*, 2010b). O₃ is primarily destroyed by photolysis (O₃+hv \rightarrow O(1 D, 3 P)+O₂) during daylight with \sim 2 minute lifetime, and by reaction with hydrogen (H+O₃ \rightarrow OH+O₂) and oxygen (O+O₃ \rightarrow 2O₂) at night (Huang *et al.*, 2008; Smith and Marsh, 2005). The ozone photochemical equilibrium assumption, i.e., ozone loss is balanced by ozone production, is crucial for retrieving O and H concentrations (Kulikov et al., 2018; Mlynczak et al., 2007). The secondary ozone layer exhibits strong seasonal dependence, with peak O₃ mixing ratios occurring in winter (Fig. 1b) when reduced sunlight minimizes photolysis and lower H₂O limits H availability. Temperature further modulates ozone kinetics, with colder conditions enhancing O₃ by accelerating production rate and inhibiting loss rates (Smith *et al.*, 2018).

Despite these advances in understanding ozone chemistry, key questions remain regarding ozone variability drivers. Solar activity appears to suppress ozone via production of odd hydrogen and odd nitrogen species (Jia *et al.*, 2024), with solar cycle signals and long-term trends occasionally documented (Huang *et al.*, 2014; Lee and Wu, 2020). PMCs may

enhance ozone through dehydration, which is expected to reduce the H above PMCs (Siskind *et al.*, 2008; Siskind *et al.*, 2018; Siskind and Stevens, 2006). The secondary ozone layer impacts mesospheric energy budgets through competing processes, including solar radiative heating, chemical heating, and infrared cooling (Ramesh *et al.*, 2015), and the total (radiative and chemical) heating of O and O₃ is of great importance for the energy budget of upper mesosphere (Mlynczak et al., 2018; Mlynczak and Solomon, 1993).

1.3 Temperature trends and variability

80

85

Mesospheric temperatures display complex variability patterns across multiple timescales. Interannual variations (4~5 K), outweigh the 11-year solar signal (1~3 K/100 solar flux unit) and the long-term cooling trend (-1~-2 K/decade) (French *et al.*, 2020a; French *et al.*, 2020b). In the summer polar mesopause, solar signals are unexpectedly absent in temperature, presumably due to a compensating dynamical cooling effect (Karlsson and Kuilman, 2018; Qian *et al.*, 2019). A well-established CO₂-induced cooling trend prevails throughout most of the middle atmosphere, with a rate exceeding tropospheric warming magnitudes (Feofilov and Kutepov, 2012; Laštovička, 2017; Roble and Dickinson, 1989). This strong cooling is regarded as a potential indicator of climate change (Liu *et al.*, 2024; Solomon *et al.*, 2018). However, the summer polar mesopause presents a notable exception, exhibiting an unexpected warming trend that contradicts the dominant CO₂ cooling. Proposed explanations include shrinking effect (Bailey *et al.*, 2021; Dawkins *et al.*, 2023; Lübken *et al.*, 2013) and long-period vertical oscillations of temperature profile (Kalicinsky *et al.*, 2018; Offermann *et al.*, 2021), though the primary mechanism remains elusive. Stratospheric ozone recovery further complicates this picture by modulating gravity wave propagation, which subsequently affects mesospheric winds and temperatures (Smith *et al.*, 2010a; Venkateswara Rao *et al.*, 2015).

These interconnected physical and chemical processes create substantial challenges for a comprehensive understanding of the climate in upper mesosphere. This paper elucidates a systematic bottom-up mechanism, linking summer polar upwelling to interannual variability in H₂O, H, O₃, O, and temperatures. Section 2 details the satellite datasets (MLS, SABER, SOFIE) and theoretical framework, Section 3 quantifies the hemispheric climate patterns during solstice months (December/June), Section 4 discusses variability mechanism, and Section 5 summarizes key conclusions.

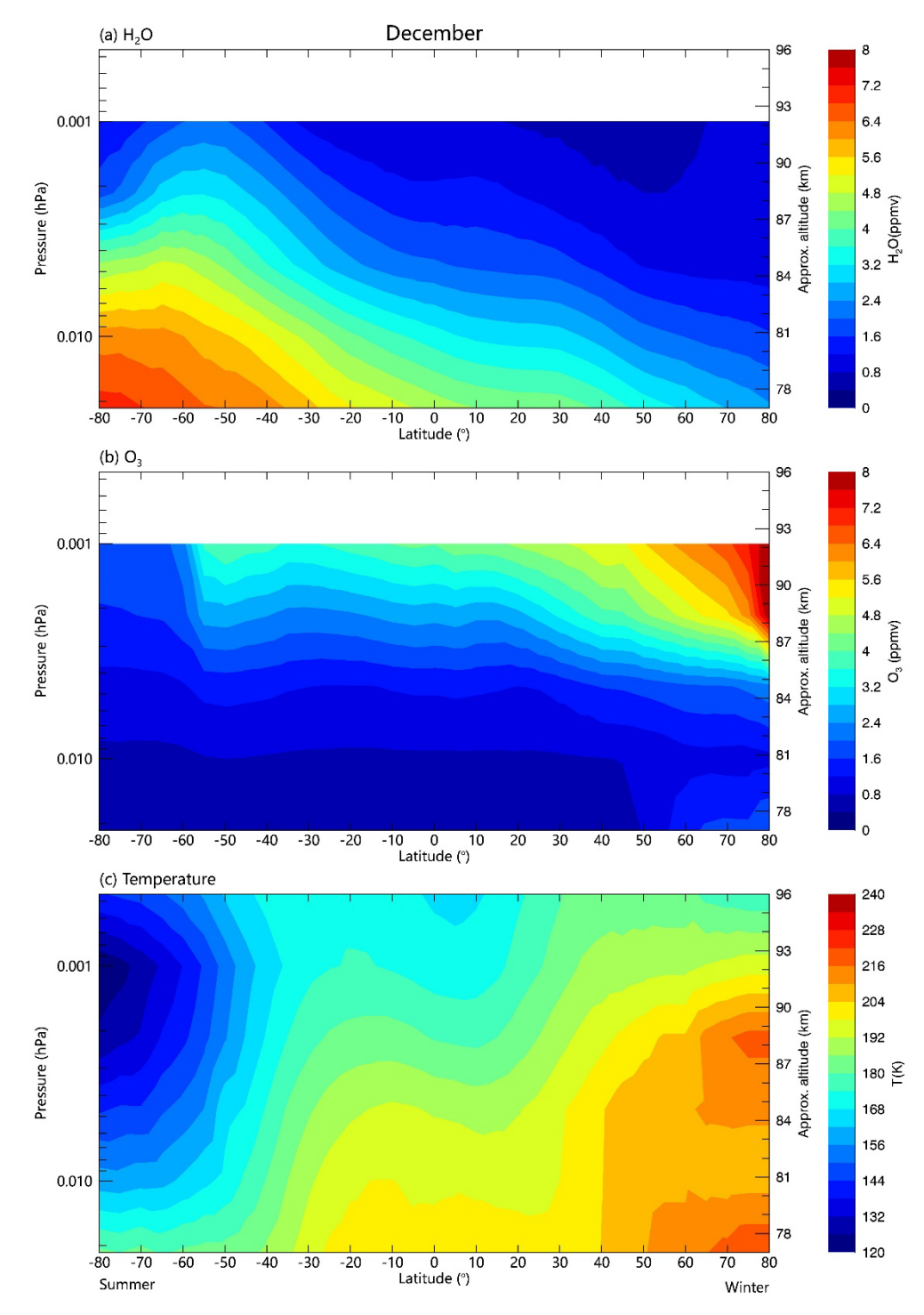


Figure 1. December climatology of (a) water vapor mixing ratio, (b) ozone mixing ration, and (c) temperature in the upper mesosphere. Data represent monthly means from MLS/Aura observations during 2004-2022.

90 2 Data and method

100

105

110

120

2.1 Multi-satellite Data

This study utilizes measurements from three satellite instruments to investigate upper mesospheric climate variability. The Microwave Limb Sounder (MLS) aboard NASA's Aura satellite, launched in July 2004, provides global atmospheric measurements between 82°N and 82°S (Jiang et al., 2007). Operating in a sun-synchronous orbit with equatorial crossings at 01:30 (ascending) and 13:30 (descending) local time, MLS delivers vertical profiles of H₂O (0.001 hPa top level recommended, 7~9 km vertical resolution, 30% precision), O₃ (0.001 hPa, 5~7 km, 35%), and temperature (0.00046 hPa, 6~12 km, 3 K). Daily mean values were generated by averaging ascending and descending orbits, focusing on zonal (5° gridded) and monthly means for interannual variability studies. Fig. 1 shows the December climatology of H₂O, O₃, and temperature observed by MLS.

The Sounding of the Atmosphere using Broadband Emission Radiometry (SABER) instrument aboard the Thermosphere, Ionosphere, Mesosphere Energetics, and Dynamics (TIMED) satellite was launched in December 2001. With an orbital inclination of 74.1°, SABER's limb scan provides latitude coverage alternating between 83°N to 52°S (during June) and 52°N to 83°S (during December) due to its 60-day yaw cycle (Russell et al., 1999). This 60-day yaw cycle allows interannual comparison by maintaining stable latitude and local time coverage for a given month across different years. We used TIMED/SABER version 2.07 data between 0.01 and 0.003 hPa from 2002 to 2019, including temperature (Remsberg et al., 2008), ozone (Rong et al., 2009; Smith et al., 2013), atomic oxygen (Mlynczak et al., 2013; Mlynczak et al., 2018), and atomic hydrogen (Mlynczak et al., 2014).

The Solar Occultation for Ice Experiment (SOFIE) instrument onboard the Aeronomy of Ice in the Mesosphere (AIM) satellite was launched on 25 April 2007 into a sun-synchronous polar orbit (Russell III *et al.*, 2009). SOFIE covers latitudes between 65° and 82°, with particular focus on ~70° latitude during PMC seasons. Using solar occultation measurements, SOFIE obtains vertical profiles of PMC properties, temperature, water vapor, and ozone (Gordley *et al.*, 2009; Hervig *et al.*, 2009). SOFIE provides datasets for 8 PMC seasons (from 2007 to 2014) in the northern hemisphere (NH) and 7 PMC seasons (from 2007/2008 to 2013/2014) in the southern hemisphere (SH), after which SOFIE measurements shifted to lower latitudes where PMCs typically do not form.

115 2.2 Bottom-up control mechanism framework

Our methodology examines the responses of mesospheric variables (H_2O , H, O_3 , O, T90) to upwelling on interannual timescales. Since direct observations of summer polar upwelling are unavailable, we use temperature at ~80 km ($T80_s$) as a proxy, based on its relationship with adiabatic cooling. Figure 2 illustrates the conceptual framework for how summer polar upwelling drives interannual climate variability during solstice months through the interconnected pathways in the "upwelling— $H_2O(H)$ — $O_3(O)$ —T90" chain:

(1) H₂O/H variability. Upwelling produces both hydration that occurs below PMCs through direct transport of H₂O by upwelling, and dehydration above PMCs through a "cold-trap effect". Explicitly, adiabatic cooling from upwelling lowers T80_S promotes water vapor condensation into ice particles, thereby reduces upward H₂O transport and causes dehydration above PMCs (Zhang *et al.*, 2025a). While similar to the conventional freeze-drying effect, the cold-trap effect shows distinct characteristics that we discuss later in section 4.1. Meridional winds then transport both the hydration and dehydration toward the winter hemisphere. Atomic hydrogen H, produced through H₂O photolysis, consequently varies in synchrony with H₂O in both hemispheres.

125

130

135

- (2) O₃/O responses. O₃ abundance is negatively influenced by H₂O through H acting as a primary O₃ sink (Zhang *et al.*, 2025b). Upwelling therefore enhances summer-hemisphere O₃ through dehydration while it inhibits winter-hemisphere O₃ through hydration. Additionally, the adiabatic cooling of upwelling directly enhances summer-hemisphere O₃ through temperature-dependent ozone kinetics. Following the ozone photochemical equilibrium assumption, the O varies in phase with O₃ and is similarly controlled by summer polar upwelling.
- (3) Temperature modulation. In the upper mesosphere, the total (radiative and chemical) heating of O and O₃ significantly influences the energy budget, creating a positive correlation between O/O₃ and T90. Since upwelling oppositely controls O₃/O in the two hemispheres, it produces an anti-phase temperature response: T90_S in the summer polar region shows a negative correlation with T80_S, while T90_W in winter hemisphere exhibits a positive correlation with T80_S.

This theoretical framework enables a quantitative evaluation of variable sensitivities to T80_s through inter-satellite comparisons, to establish robust causal relationships in the observed climate variability.

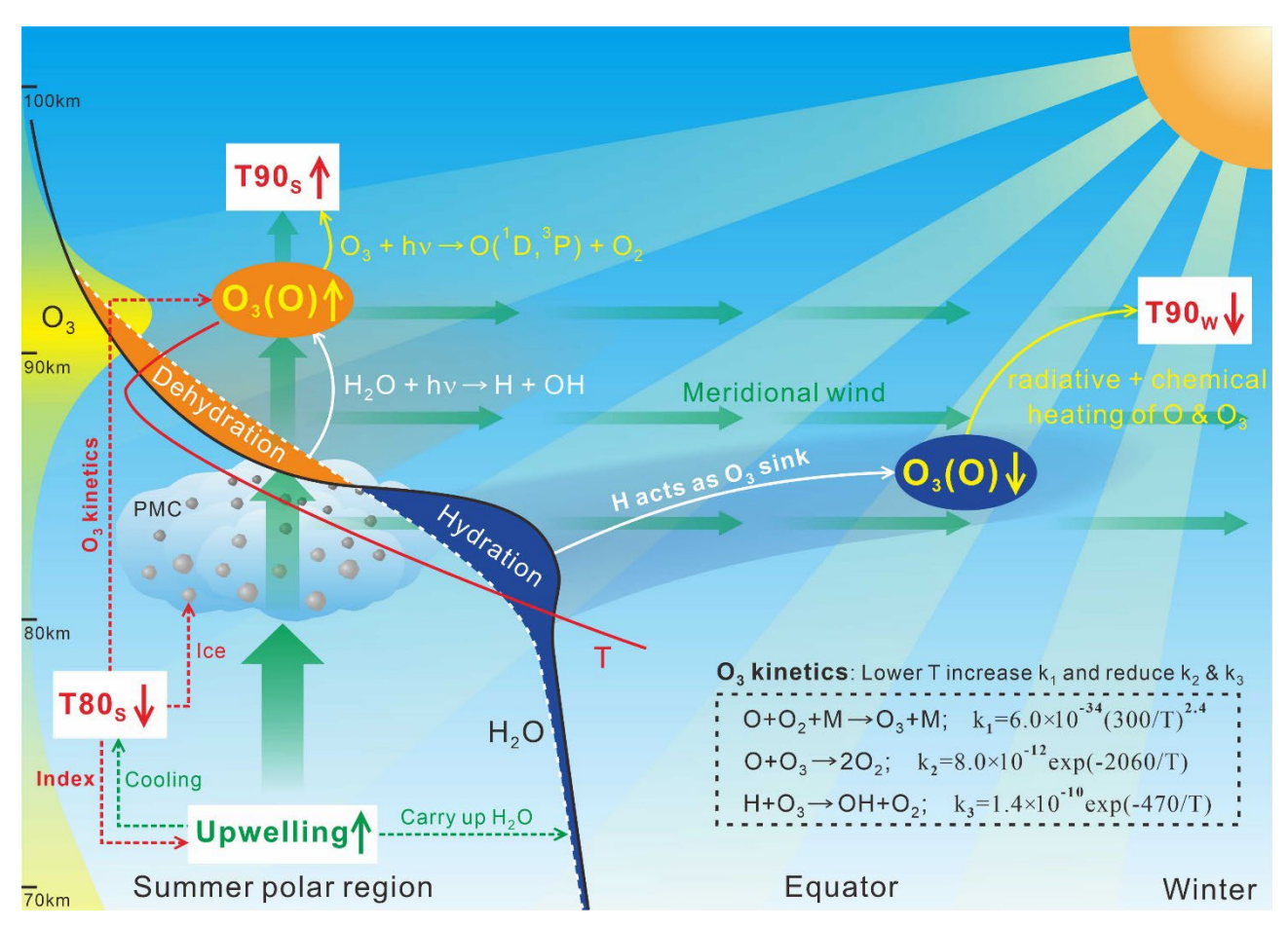


Figure 2. Schematic diagram of the bottom-up control mechanism in solstice months, showing how summer polar upwelling controls interhemispheric climate variability through coupled dynamical and chemical processes. Key pathways include: (1) winter-hemisphere hydration is induced by summer polar upwelling in combination with meridional transport, and summer-hemisphere dehydration is governed by the cold-trap effect; (2) subsequent modulation of O₃ through H-driven ozone loss and temperature-dependent ozone kinetics, with O varying in pace with O₃ due to the ozone photochemical equilibrium assumption; and (3) resulting temperature (T90) variations via radiative and chemical heating of O₃/O.

3 Results

150

155

160

165

170

175

3.1 Climate patterns in December

Our analysis of MLS/Aura data reveals distinct interannual variability patterns during December (Figure 3). Using T80_S as an upwelling proxy, we observe opposing H₂O responses between hemispheres: dehydration in the summer polar mesopause (75°S-82°S) indicated by positive correlations with T80_S (R=0.93, Fig. 3a), and hydration at low latitudes (15°N-20°N) in the NH indicated by negative correlations (R=-0.84, Fig. 3e). The H₂O patterns drive corresponding O₃ variations through chemical interaction, with T80_S showing negative correlations (R=-0.91) with O₃ at 0.001 hPa (65°S-75°S, Fig. 3b) but positive correlations (R=0.94) at 0.002 hPa (15°N-20°N, Fig. 3f). Temperature responses exhibit clear hemispheric antisymmetry, with T90_S at 0.0046 hPa (65°S-75°S) negatively correlated (R=-0.92, Fig. 3d) and T90_W at 0.001 hPa (15°N-20°N) positive correlated (R=0.80, Fig. 3h) with T80_S. In addition, the standard deviations of these variables significantly exceed their linear trends, potentially masking long-term signals.

Figure 4 shows the latitudinal extent of these relationships, with sensitivities derived from linear regression. Meridional transport extends dehydration signature to 35°S (beyond the PMC coverage) and hydration to 35°N (Fig. 4a), while O₃ responses show comparable latitudinal ranges (Fig. 4b). SABER observations corroborate these findings (Figure 5), though atomic hydrogen data gaps at summer high latitudes (Fig. 5a) prevent complete verification of dehydration effects. The ozone photochemical equilibrium assumption holds well, with atomic oxygen O varying in pace with O₃ (Fig. 5b, c). Mlynczak *et al.* (2018) showed that the total (radiative and chemical) heating rate of O and O₃ is ~10 Kday⁻¹ on global and annual scale (Fig. 3 therein). The relative variations of O and O₃ to T80_S in Fig. 5 are both ~4%/K, therefore the sensitivity of O/O₃ total heating rate to T80_S is roughly estimated to be ~0.4 Kday⁻¹/K, which partly explain the ~1K/K (Fig. 5d) response of T90 to T80_S.

Daily-scale SOFIE observations provide further insights (Figures 6-8). Figure 6 shows that O₃ at 90 km is bottom-up controlled by the T80_S at 79 km. It is noteworthy that in November, during which PMCs are weak and dehydration is absent, the negative correlation between O₃ and T80_S remains significant, possibly due to the temperature-dependent ozone kinetics. Summer polar O₃ near 0.01 hPa (Fig. 5b) or 80 km (Fig. 7c) is negatively correlated to T80_S, which should be attributed to ozone kinetics. As shown in Fig. 8b, O₃ below 90 km lags T80_S by zero days possibly through ozone kinetics, while O₃ above 90 km lags T80_S by ~3 days, suggesting combined kinetic and dehydration influences. However, for upper-level O₃, the relative contribution of ozone kinetics and dehydration (depletion of H) is unclear.

Fig. 7a, b shows that the H₂O above and below PMCs is both bottom-up controlled by T80_S rather than the temperature above PMC, which supports the cold-trap effect. Fig. 8a further shows that the hydration and dehydration both lag behind T80_S by about zero days, consistent with the cold-trap effect. In contrast, according to the conventional freeze-drying effect, the dehydration tends to occur prior to the hydration, with the time interval roughly equal to the lifetime of ice particle which is up to two days in simulations (not consider transport and diffusion of ice particles). In addition, T90 is positively

correlated to O_3 (Fig. 7c) and negatively correlated to $T80_8$ (Fig. 7d), with lag time of about ~ 3 days, matching the radiative and chemical heating of O_3/O .

3.2 Climate patterns in June

180

185

190

The climate patterns in June (Figures 9-12) mirror those of December, but with reduced amplitudes. The T80_s variability is weaker (1.5 K vs. 5.1 K in December), yielding smaller constituent variations and lower significance (Figs. 3, 9). SABER H responses are insignificant (Fig. 11a), while T90_s correlations weaken or disappear (Figs. 11d, 12d). MLS data show a localized hydration signal at 0.001 hPa between 70°N~80°N (Fig. 10a), possibly from PMC sublimation due to higher T90_s.

Interhemispheric transports are more pronounced in June than in December due to differences in gravity wave forcing of the circulation (Smith *et al.*, 2011). The enhanced meridional transport extends H₂O influences to 40°S~50°S, affecting O₃ and T90_W in the winter high-latitudes (Fig. 10). Downward winds in the winter polar region generally result in the lowest H₂O levels near solstice, although vertical winds and diffusion can increase winter polar H₂O above 90 km (Lossow et al., 2009). Whether the summer polar upwelling in June could influence the winter high-latitude climate through interhemispheric H₂O transport is an interesting question.

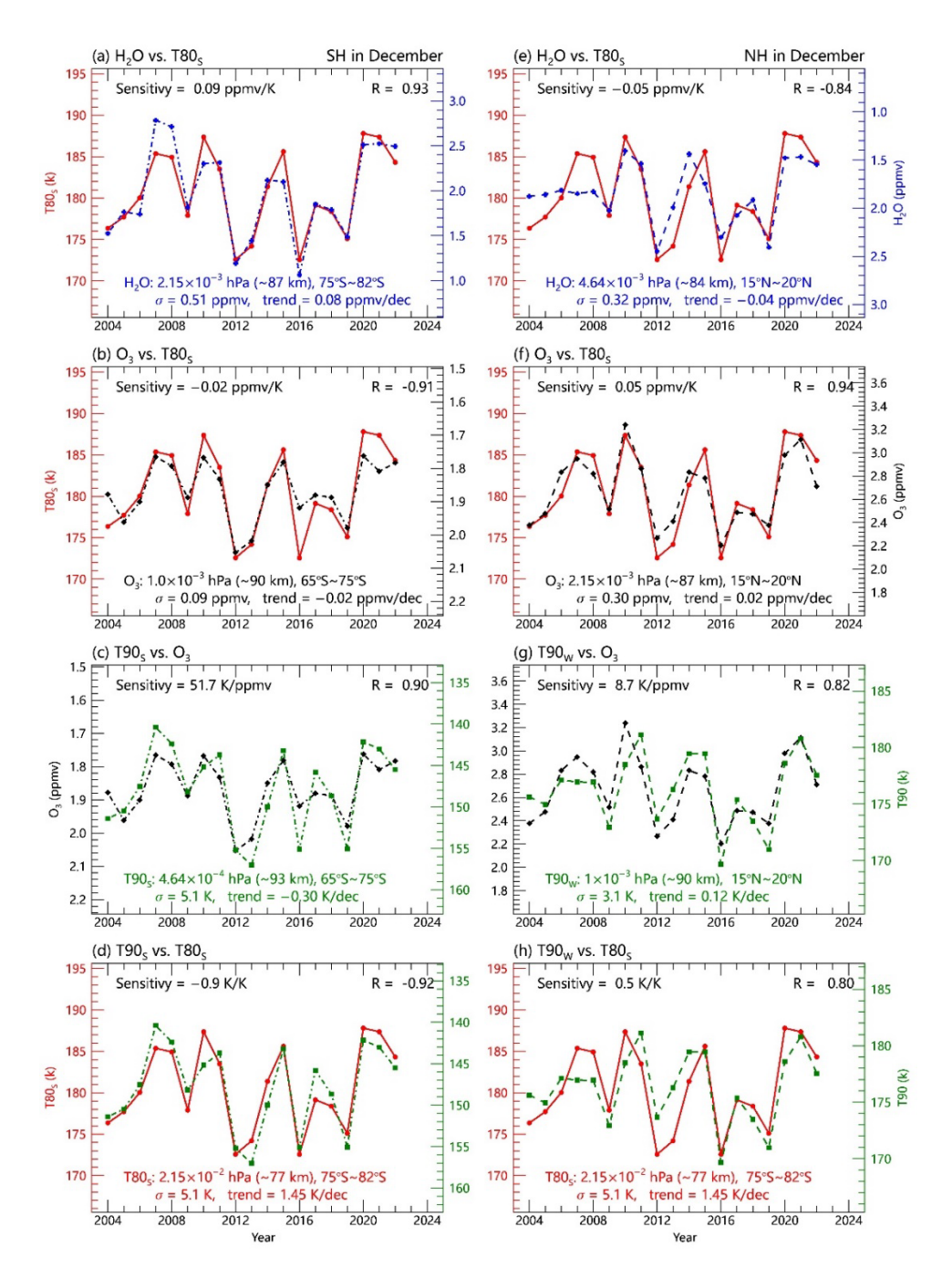


Figure 3. Hemispheric responses of mesospheric (a, e) H₂O, (b, f) O₃, and (d, h) T90 to upwelling variability (indicated by T80_S) during December, showing anti-phase behavior between (left) summer and (right) winter hemispheres. Panels (c, g) show O₃-T90 correlations. All plots display monthly and zonal means from MLS/Aura observations during 2004-2022, with correlation coefficients (R), sensitivities, standard deviations (σ), and trends derived from linear regression analysis. The opposing H₂O responses reflect hydration (winter hemisphere, negative correlation) and dehydration (summer hemisphere, positive corelation), while O₃ and T90 variations demonstrate the consequent chemical and thermal feedbacks.

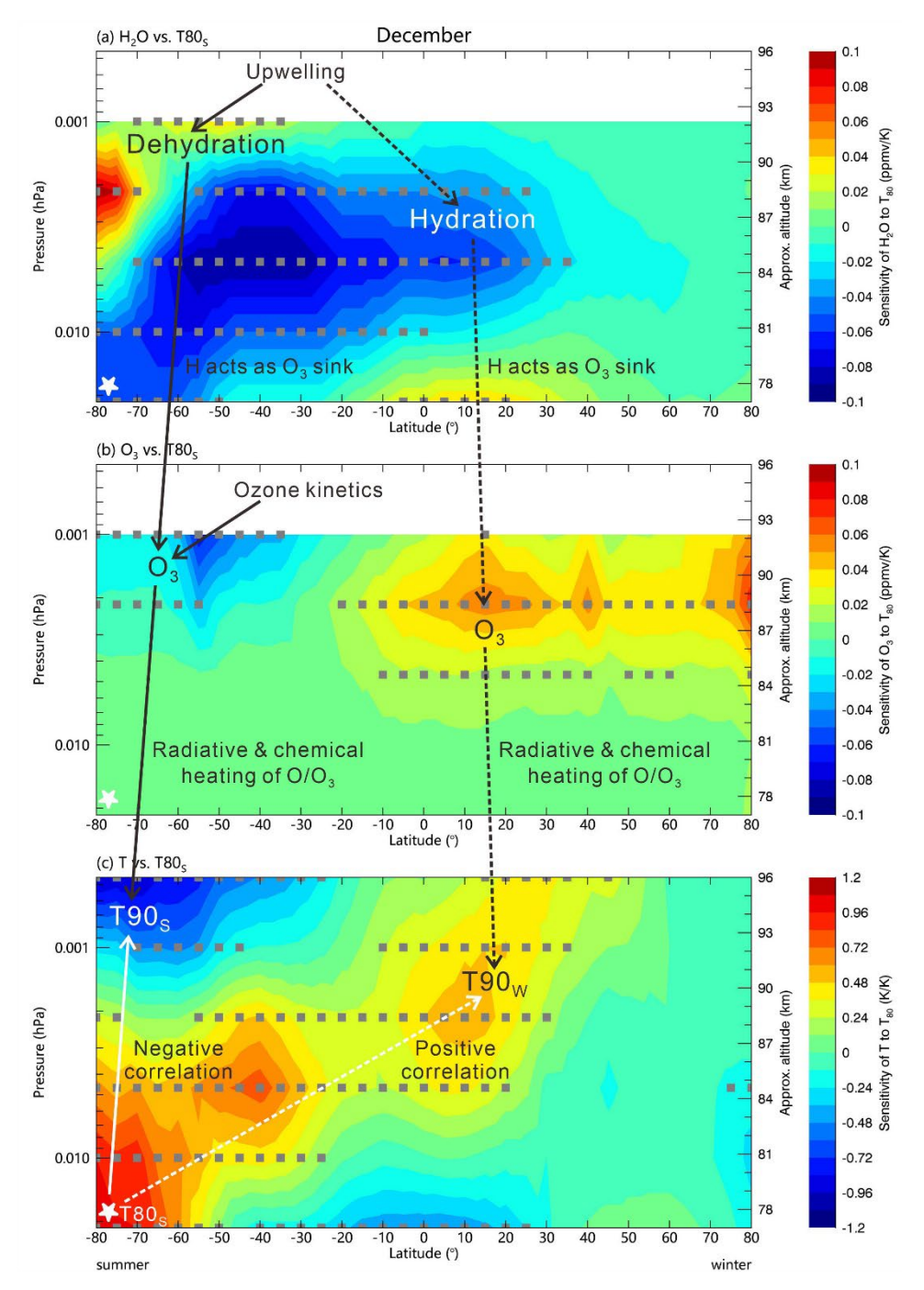


Figure 4. Spatial patterns of bottom-up control processes during December showing (a) H₂O hydration (blue) and dehydration (red) response to upwelling (indicated by T80_S, white stars), (b) corresponding O₃ variations in both hemispheres, and (c) resultant temperature (T90) changes driven by radiative and chemical heating. Sensitivities of variables to T80_S derived from linear regression of MLS/Aura data during 2004-2022 show significant anti-phase relationships between hemispheres. Gray points make the 0.95 significance level.

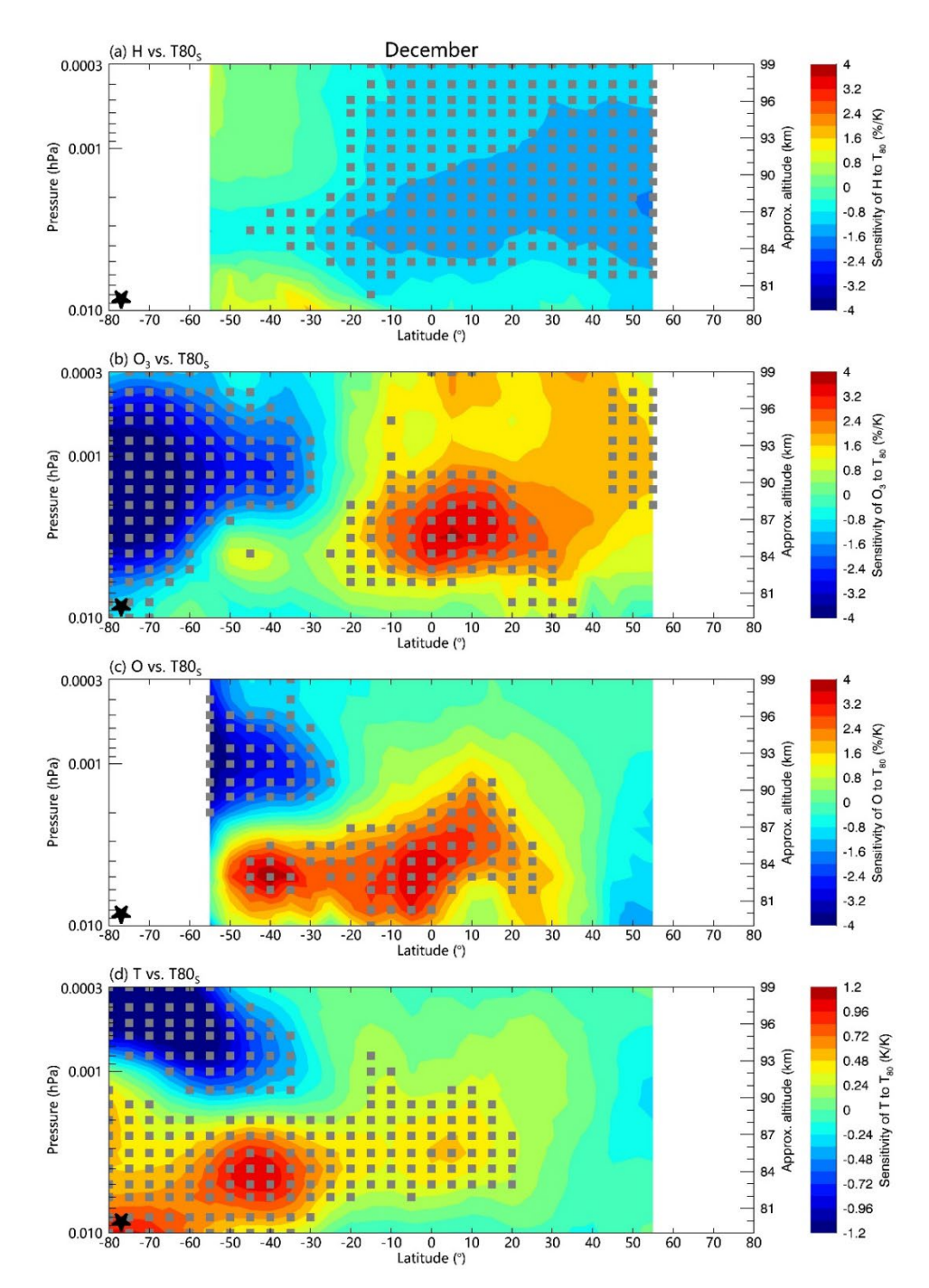


Figure 5. Bottom-up control of atmospheric constituents in December from SABER observations during 2002-2019. (a) H response to upwelling (indicated by T80_S, black stars at 75°S~83°S, 0.01 hPa level). (b) O₃ and (c) O variations, both demonstrating hemispheric anti-symmetry in their sensitivity to T80_S. (d) Resultant temperature responses showing a positive correlation between T90_W and T80_S and a negative correlation between T90_S and T80_S through the radiative and chemical heating of O and O₃. All sensitivities (relative responses in unit of %/K) have been derived from linear regression analysis of monthly data, with consistent upwelling-driven patterns across variables.

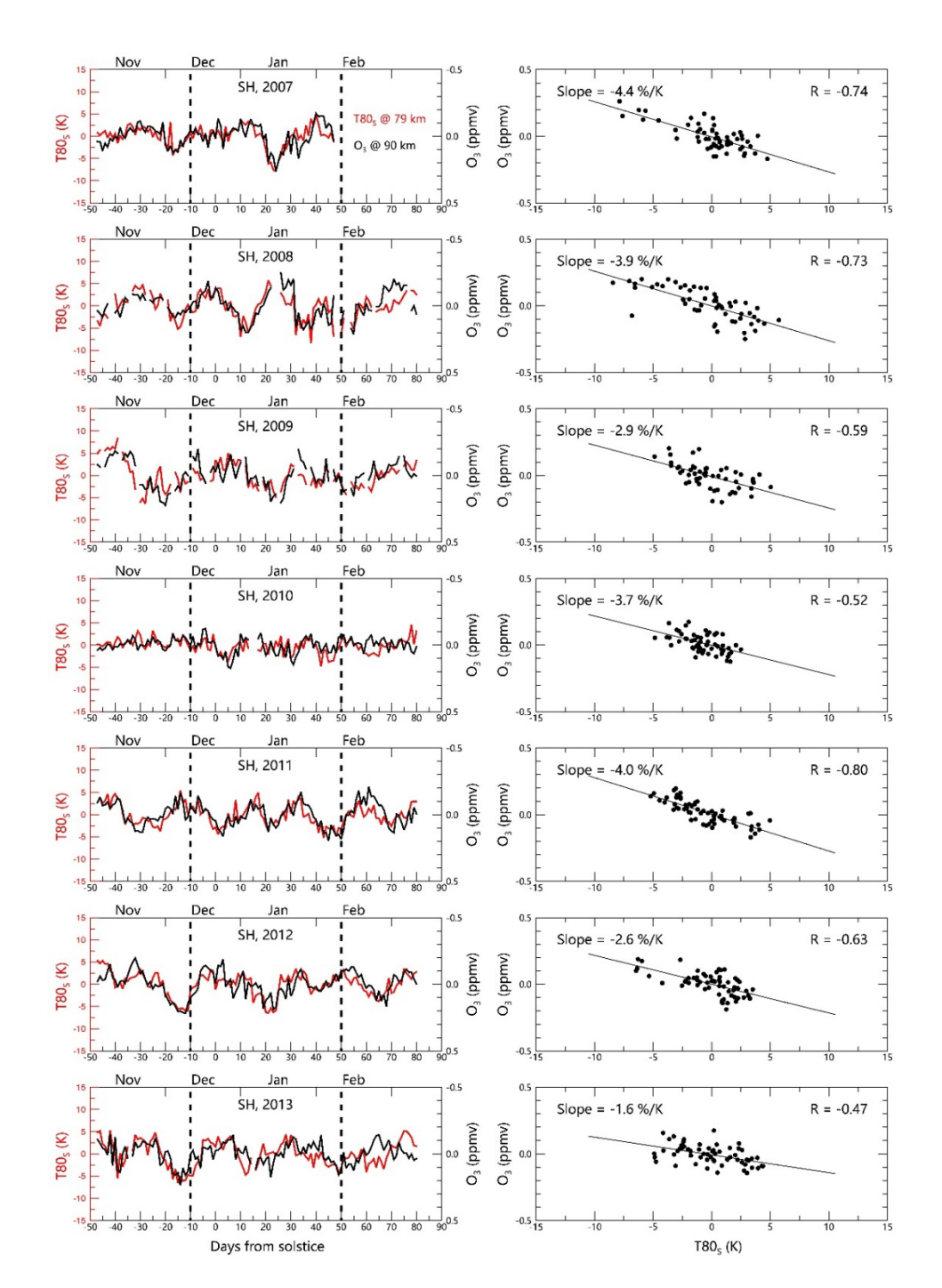


Figure 6. Temporal relationship between T80_S and O₃ variations from SOFIE/AIM observations for the SH PMC seasons during 2007-2013. (Left) Daily time series of T80_S at 79 km (red) and O₃ at 90 km (black) at ~70°S, with 35-day running mean removed. (Right) Correlation coefficients between T80_S and O₃ for each PMC season during -10 to 50 days relative to solstice, demonstrating consistent negative relationships (mean R=-0.64) that highlight the bottom-up control of upwelling on ozone chemistry.

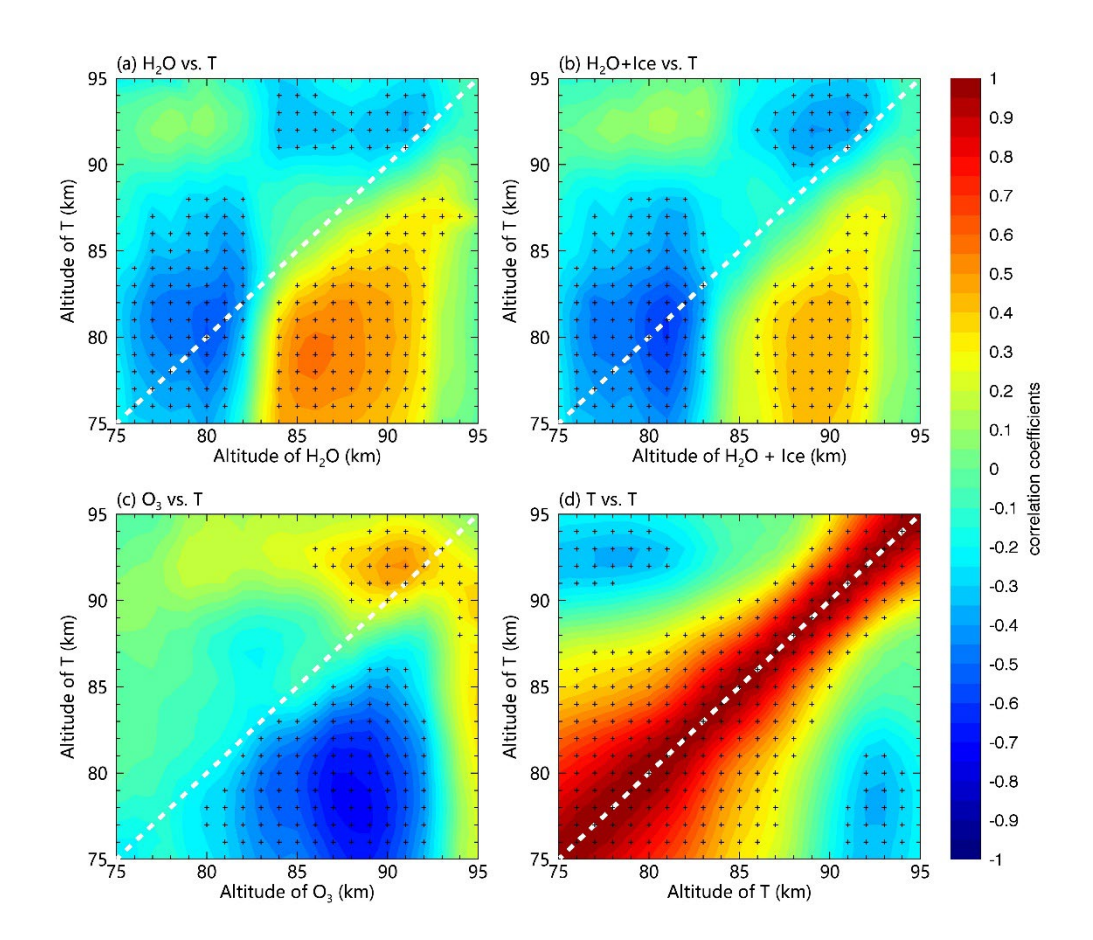


Figure 7. Daily-scale bottom-up control processes observed by SOFIE at ~70°S for the SH PMC seasons during 2007-2013.

(a) H₂O above and below 83 km are both subject to the control of T80_S rather than local temperatures. (b) Combined H₂O and ice content demonstrate similar T80_S dependence. (c) Anti-correlation between O₃ and T80_S, accompanied by positive O₃-T90 relationship. (d) Negative correlation between T90_S and T80_S. Correlation coefficients are calculated for -10 to 50 days relative to solstice (35-day running mean removed), with the 0.95 significance level marked by dots.

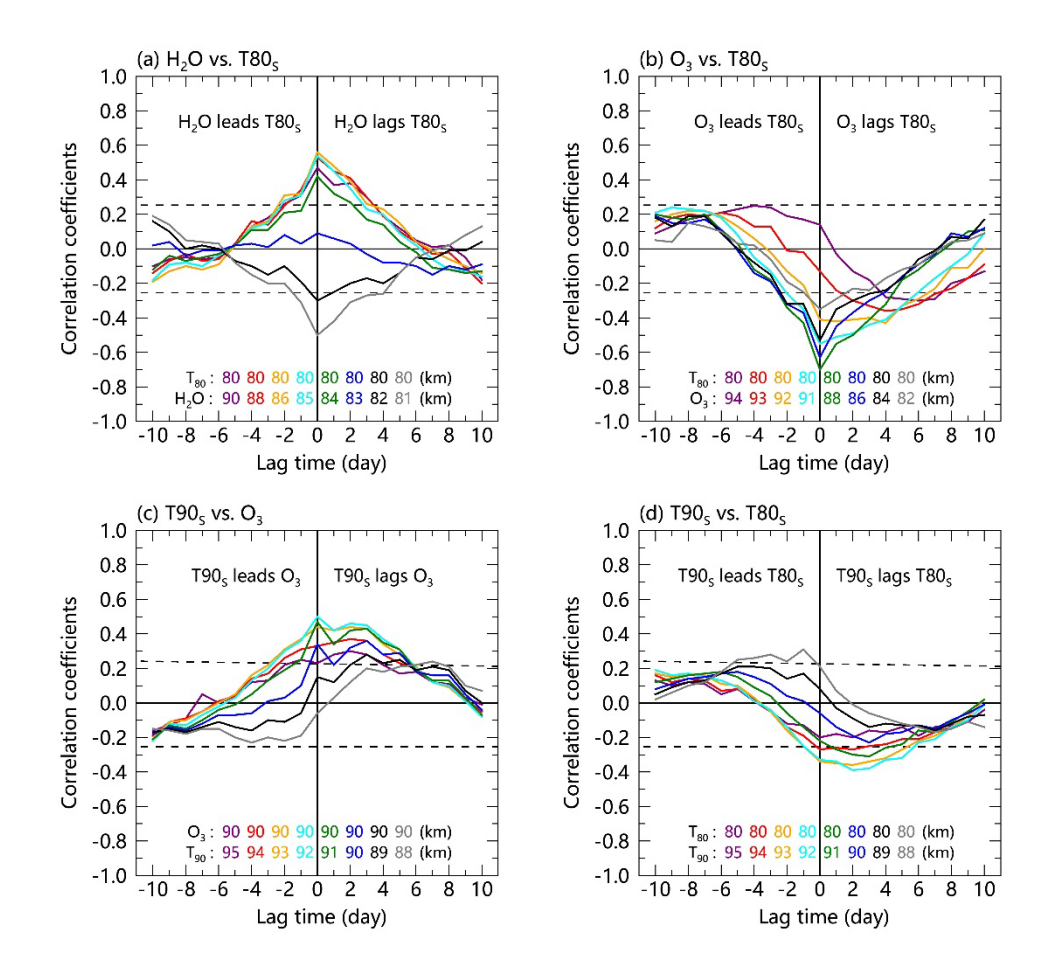


Figure 8. Time-lag analysis of bottom-up control processes from SOFIE observations at ~70°S for the SH PMC seasons during 2007-2013. (a) Immediate response (zero-day lag) of both hydration (negative H₂O-T80_S correlation) and dehydration (positive H₂O-T80_S correlation) to upwelling. (b) O₃ response showing altitude-dependent lags to T80_S. (c) T90_S lags behind O₃ by ~3 days, possibly due to the radiative and chemical heating. (d) T90_S lags after T80_S by ~3 days, indicating the cumulative response time of the full upwelling-H₂O-O₃-T90_S chain. Correlation coefficients are calculated similar to Figs. 6-7, with dashed lines marking the 0.95 significance level.

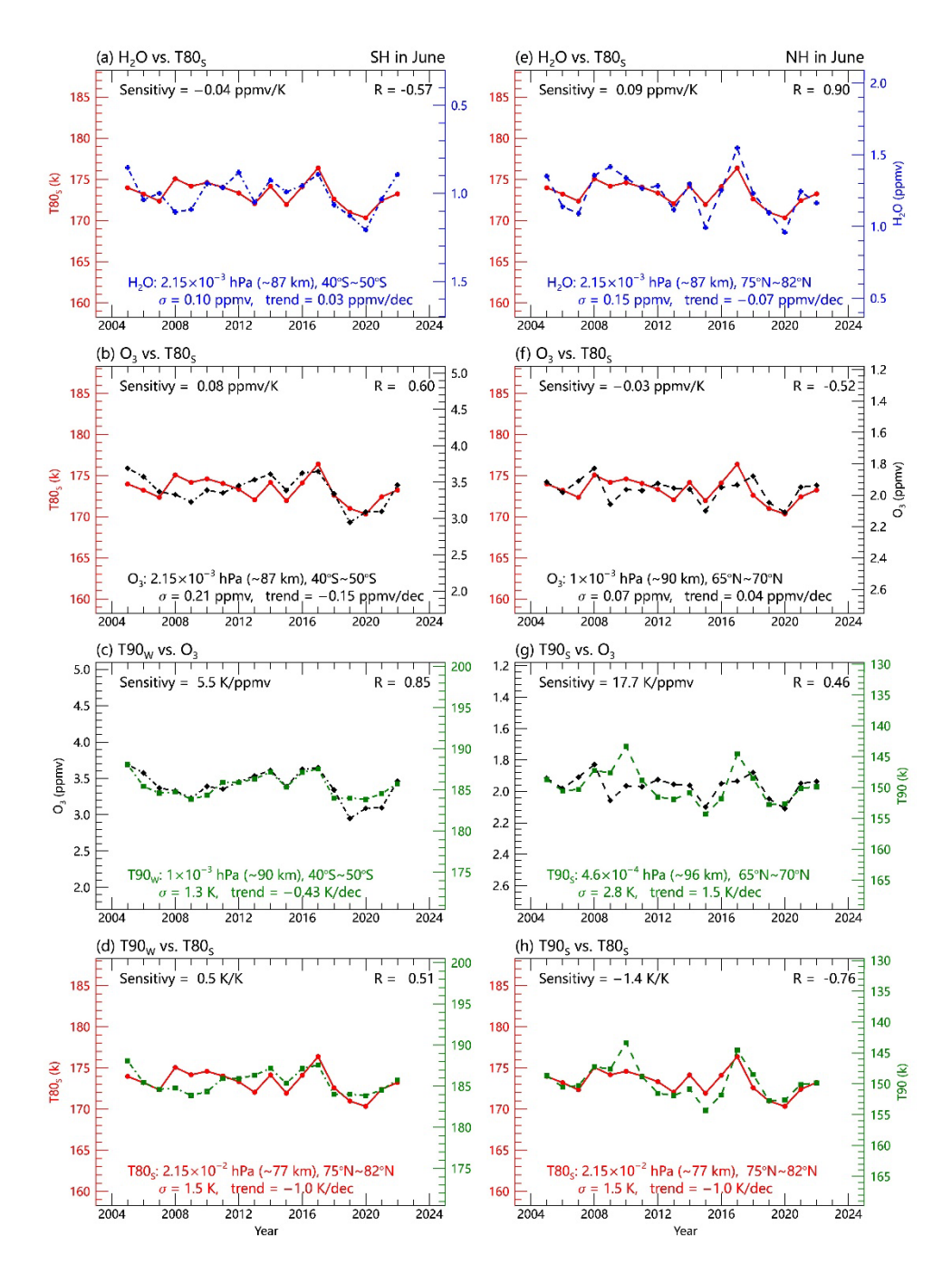


Figure 9. Hemispheric responses of mesospheric (a, e) H₂O, (b, f) O₃, (d, h) T90 to upwelling variability (indicated by T80_S) during June, showing analogous but weaker anti-phase behavior compared to December (Fig. 3). Panels (c, g) show O₃-T90 correlations. Note the reduced amplitude of T80_S standard deviation (1.5 K in June vs. 5.1 K in December) and weaker correlations in the June patterns.

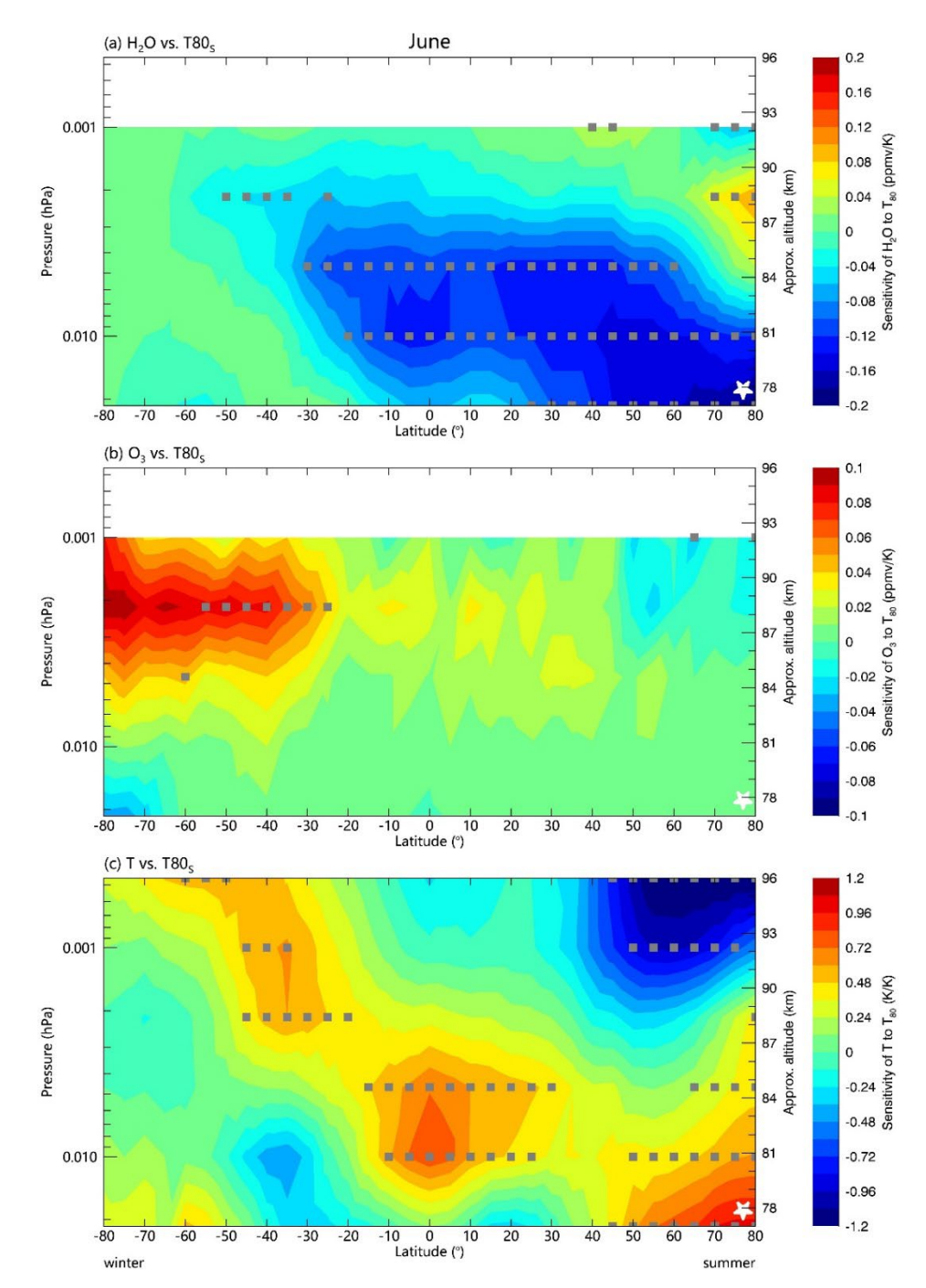


Figure 10. Spatial patterns of bottom-up control processes during June showing (a) H₂O, (b) O₃, and (c) temperature responses to upwelling (indicated by T80_S, white stars), analogous to but weaker than December patterns (Fig. 4). Sensitivities derived from linear regression of MLS/Aura data (2004-2022) show reduced but still significant anti-phase relationships between hemispheres compared to December. Gray dots mark the 0.95 significance level. Note the responses of variables in winter hemisphere extend to ~50°S in June.

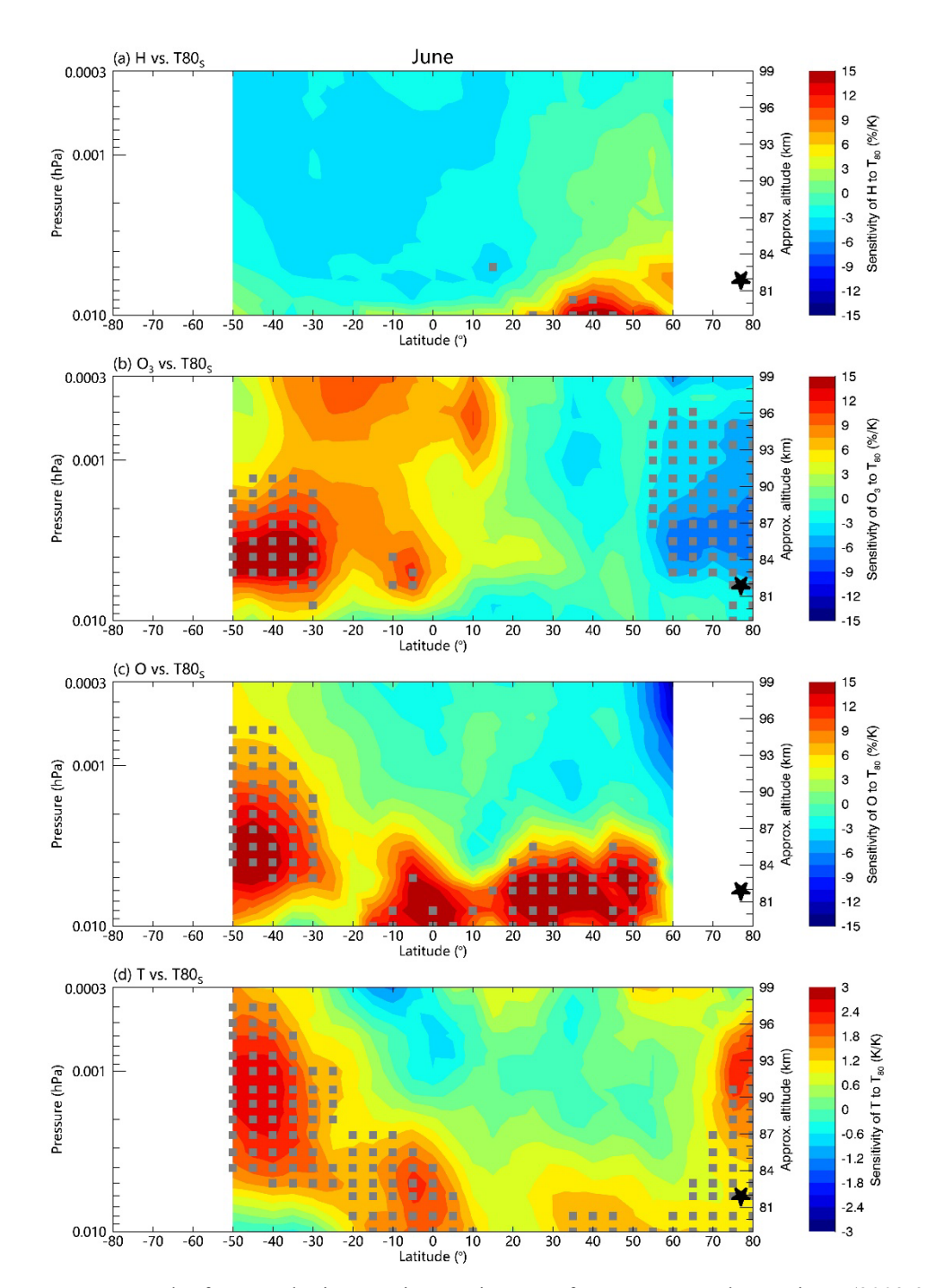


Figure 11. Bottom-up control of atmospheric constituents in June from SABER observations (2002-2019), showing analogous but weaker responses than December (Fig. 5). (a) H shows insignificant response to upwelling (indicated by T80_S, black stars at 75°N-83°N, 0.006 hPa). (b) O₃ and (c) O variations exhibit reduced hemispheric anti-symmetry in sensitivity to T80_S. (d) The positive T90_W responses in wither hemisphere maintain, but the negative T90_S responses disappear. All sensitivities have been derived from linear regression analysis of monthly data.

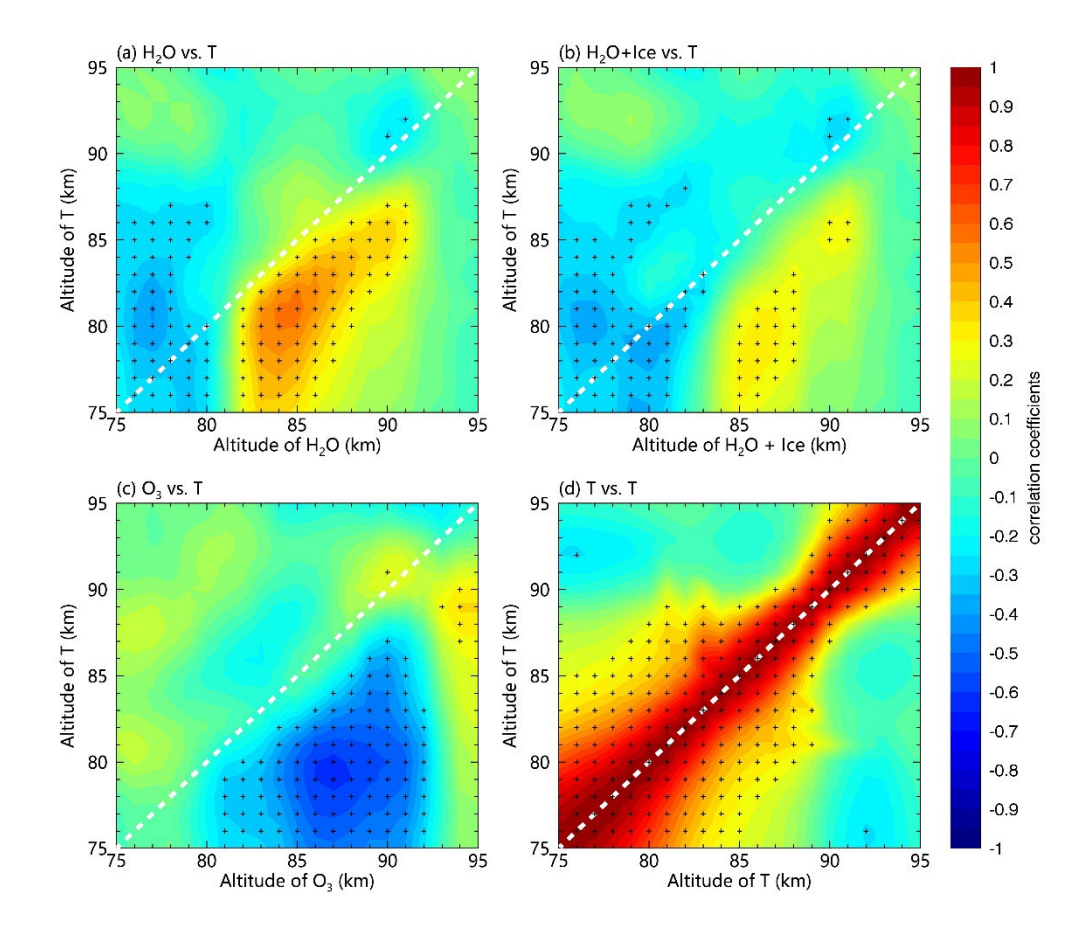


Figure 12. Daily-scale bottom-up control processes from SOFIE/AIM observations for the NH PMC seasons during 2007-2014. (a) H₂O in NH shows weaker control by T80_S compared to that in SH (Fig. 7). (b) Combined H₂O and ice content demonstrating similar but less pronounced T80_S dependence. (c) Anti-correlation between O₃ and T80_S with reduced O₃-T90_S relationship. (d) Weaker negative relationship between T90_S and T80_S. Correlation coefficients calculated for -10 to 50 days relative to solstice (35-day running mean removed), with black dots marking the 0.95 significance level. Note the generally weaker responses compared to SH observations in Fig. 7.

4 Discussion

260

265

270

275

280

285

4.1 H₂O/H variability mechanisms

Our results demonstrate it is the summer polar upwelling that fundamentally drives the interannual variability of both hydration and dehydration through two distinct pathways: (1) direct upward transport of H₂O by upwelling combined with meridional wind transport creates hydration in the winter hemisphere; and (2) adiabatic cooling associated with upwelling enhances ice particle growth that blocks upward H₂O transport, causing dehydration above PMC in the summer hemisphere.

The cold-trap effect differs from the conventional freeze-drying effect in several ways. While freeze-drying effect describes a top-down process dominated by ice particle sedimentation, the cold-trap effect represents a bottom-up process driven primarily by upwelling dynamics. Sedimentation of ice particles plays a dominant role in the freeze-drying effect, however, it is unnecessary in the cold-trap effect (Zhang *et al.*, 2025a). Importantly, the cold-trap effect produces simultaneous hydration and dehydration. In contrast, the freeze-drying effect involves dehydration prior to hydration, with a time lag (estimated as the ice particle lifetime) of up to two days. Particularly, if PMCs are weak or absent and ice particles could not block upward H₂O transport, hydration could even occur in the absence of dehydration, inconsistent with the freeze-drying effect.

It should be emphasized that we are not attempting to demonstrate that the freeze-drying effect is incorrect. Instead, the two mechanisms should be complementary rather than contradictory. The freeze-drying effect has been verified by simulations for describing PMC microphysical processes at local scales, while the cold-trap effect better explains the global-scale H₂O redistribution patterns, especially the H₂O in the winter hemisphere. Additionally, the parameterization of freeze-drying effect is unavailable until now, due to the complexity in PMC simulations. In contrast, the cold-trap effect is much simpler, the interannual variability of hydration/dehydration is only dependent on the T80_S. The limited H variability detected in SABER data (Figs. 5a, 11a) may reflect both measurement uncertainties in H retrieval and gaps in spatial coverage in high-latitude regions where dehydration effects are strongest.

4.2 O₃/O response pathways

Upwelling forcing drives distinct hemispheric patterns in O₃ variations. In the winter hemisphere, hydration-driven increases in H abundance lead to enhanced O₃ destruction. In the summer hemisphere, however, O₃ increases via two pathways: reduced H abundance due to dehydration and temperature-dependent ozone kinetics caused by adiabatic cooling.

Our vertical analysis shows that these processes operate at different altitudes (Figs. 5b, 7c). Below 85 km, where dehydration is absent, temperature-dependent ozone kinetics dominate O₃ abundance, while above 85 km both dehydration and ozone kinetics contribute, with their relative contribution remaining unclear. In addition, the lag time of O₃ to T80_S differs for varying altitudes (Fig. 8b), which may be useful for identifying the two pathways.

4.3 Temperature modulation processes

The anti-phase temperature responses between hemispheres (T90_W and T90_S) reflect the combined effect of dynamical processes and O/O₃ heating. In the winter hemisphere, based on the known radiative and chemical heating rate (~10 K/day on global and annual scale) of O/O₃, the 3~4%/K sensitivity of O₃ and O in low latitudes to T80_S (Fig. 5b, c) approximately explains the observed ~0.5 K/K sensitivity of T90_W to T80_S (Fig. 5d).

The summer hemisphere presents a more complex scenario involving competing processes. The O₃ concentration in summer polar region is very low due to the destruction by sunlight and H₂O (Fig. 1b), while the O concentrations do not differ much between the summer and winter hemispheres. The high sensitivity of T90_S to O₃ (51.7 K/ppmv, Fig. 3c) in December is likely unrealistic. O-heating likely dominates the interannual variability of T90_S, with O₃-heating playing a minor role.

Another explanation is that a potential downwelling may result in higher $T90_S$ by adiabatic heating and higher O concentration by downward transports, which further increase O_3 . The zonal winds change direction above the mesopause height, and gravity waves that induce upwelling near 80 km tend to cause downwelling at altitudes above the mesopause. In this scenario, the positive correlation between $T90_S$ and O/O_3 results from vertical winds rather than solar or chemical heating. However, Fig. 8c, d shows that the $T90_S$ lags behind O_3 and $T80_S$ by ~ 3 days, ruling out pure dynamical explanations. Fig. 4c and Fig. 5d shows that the $T90_S$ at latitudes as low as $30^\circ S$ are negatively correlated with $T80_S$, which should not be attributed to the adiabatic heating of downwelling. Moreover, shrinking effect may explain the negative correlation between $T90_S$ and $T80_S$ through the vertical shift of the temperature profile. However, the MLS and SABER results are presented on pressure levels rather than geometric heights, not supporting a shrinking effect as the major driver for the interannual variability of $T90_S$. In addition, $T90_S$ lags behind $T80_S$ by ~ 3 days (Fig. 8d), inconsistent with the shrinking effect on the daily scale.

310 5 Conclusion

295

300

305

315

320

This study establishes that summer polar upwelling serves as the primary driver of interannual variability in the upper mesospheric $H_2O(H)$, $O_3(O)$, and T90 through a bottom-up mechanism. Our findings build a simple picture for understanding the interhemispheric anti-phase climate of the upper mesosphere, revealing three key aspects of dynamical-chemical interactions: First, we demonstrate that the summer polar upwelling drives the global-scale interannual H_2O variability, namely the hydration in the winter hemisphere and dehydration in the summer hemisphere. Second, owing to the negative modulation of O_3 by H_2O and the ozone photochemical equilibrium assumption, the winter-hemisphere O_3/O decreases due to the hydration-induced depletion of H, while the summer-hemisphere O_3/O increases due to combined effects of dehydration and temperature-dependent ozone kinetics. Third, because of the radiative and chemical heating of O_3/O , there is a positive correlation between the winter-hemisphere O_3/O and O_3/O , there is a positive correlation between the winter-hemisphere O_3/O and O_3/O , and O_3/O and

Several important questions remain unresolved and need further investigation. Summer polar upwelling plays a pivotal role in the bottom-up control mechanism, while the pronounced hemispheric difference in the interannual T80_s variability (5.1 K in December, 1.5 K in June) lacks a detailed explanation. Given the importance of H₂O for mesospheric climate, the relationship between our proposed cold-trap effect and conventional, well-established freeze-drying effect should be a priority for further study. Similarly, the relative contribution of dehydration versus ozone kinetics to summer-hemisphere O₃ enhancement require quantification. Alternative explanations for the interannual T90_s variability, including shrinking effect and adiabatic heating of gravity wave-driven downwelling, cannot fully account for the observed patterns, but may make some contribution. These advances will further elucidate mesospheric climate variability while improving the physical basis for interpreting long-term trends in this intricate atmospheric region.

330

325

Data Availability. The MLS Level 2, version 5 data are available for download from the NASA GES DISC website. Specifically, the MLS water vapor data can be accessed at https://disc.gsfc.nasa.gov/datasets/ML2H2O 005/summary, the https://disc.gsfc.nasa.gov/datasets/ML2O3 005/summary, ozone data at and the data temperature at https://disc.gsfc.nasa.gov/datasets/ML2T 005/summary. The quality document of MLS available https://mls.jpl.nasa.gov/data/v5-0 data quality document.pdf. The SABER data version 2.07 of temperature, ozone, atomic oxygen, and atomic hydrogen can be download from https://data.gats-inc.com/saber/Version2 0/SABER atox/. The PMC 340 data from SOFIE/AIM are available from the SOFIE website (http://sofie.gats-inc.com/sofie/index.php).

Author Contributions. LZ, ZL, and BT conceived the idea together. LZ analyzed the data and drafted the manuscript. ZL and BT revised the paper.

Competing Interests. The authors declare that they have no conflict of interests.

Acknowledgements. We are especially grateful to the MLS, SABER, and SOFIE program for providing us with the long-range and high-quality data.

Financial support. This research has been supported the National Natural Science Foundation of China (42025602 and 41905059).

References

355

370

- Bailey, S. M., Thurairajah, B., Hervig, M. E., Siskind, D. E., Russell, J. M., and Gordley, L. L.: Trends in the polar summer mesosphere temperature and pressure altitude from satellite observations, J. Atmos. Sol.-Terr. Phy., 220, 105650, https://doi.org/10.1016/j.jastp.2021.105650, 2021.
 - Bardeen, C. G., Toon, O. B., Jensen, E. J., Hervig, M. E., Randall, C. E., Benze, S., Marsh, D. R., and Merkel, A.: Numerical simulations of the three-dimensional distribution of polar mesospheric clouds and comparisons with Cloud Imaging and Particle Size (CIPS) experiment and the Solar Occultation For Ice Experiment (SOFIE) observations, J. Geophys. Res.-Atmos., 115, https://doi.org/10.1029/2009JD012451, 2010.
 - Dawkins, E. C. M., et al.: Solar Cycle and Long-Term Trends in the Observed Peak of the Meteor Altitude Distributions by Meteor Radars, Geophys. Res. Lett., 50, e2022GL101953, https://doi.org/10.1029/2022GL101953, 2023.
 - Feofilov, A. G., and Kutepov, A. A.: Infrared Radiation in the Mesosphere and Lower Thermosphere: Energetic Effects and Remote Sensing, Surv. Geophys., 33, 1231-1280, https://doi.org/10.1007/s10712-012-9204-0, 2012.
- Fiedler, J., and Baumgarten, G.: Solar and lunar tides in noctilucent clouds as determined by ground-based lidar, Atmos. Chem. Phys., 18, 16051-16061, https://doi.org/10.5194/acp-18-16051-2018, 2018.
 - French, W. J. R., Klekociuk, A. R., and Mulligan, F. J.: Analysis of 24 years of mesopause region OH rotational temperature observations at Davis, Antarctica Part 2: Evidence of a quasi-quadrennial oscillation (QQO) in the polar mesosphere, Atmos. Chem. Phys., 20, 8691-8708, https://doi.org/10.5194/acp-20-8691-2020, 2020a.
- French, W. J. R., Mulligan, F. J., and Klekociuk, A. R.: Analysis of 24 years of mesopause region OH rotational temperature observations at Davis, Antarctica Part 1: long-term trends, Atmos. Chem. Phys., 20, 6379-6394, https://doi.org/10.5194/acp-20-6379-2020, 2020b.
 - Gao, H., Li, L., Bu, L., Zhang, Q., Tang, Y., and Wang, Z.: Effect of Small-Scale Gravity Waves on Polar Mesospheric Clouds Observed From CIPS/AIM, J. Geophys. Res.-Space, 123, 4026-4045, https://doi.org/10.1029/2017JA024855, 2018.
 - Gordley, L. L., et al.: The solar occultation for ice experiment, J. Atmos. Sol.-Terr. Phy., 71, 300-315, https://doi.org/10.1016/j.jastp.2008.07.012, 2009.
 - Gumbel, J., and Karlsson, B.: Intra- and inter-hemispheric coupling effects on the polar summer mesosphere, Geophys. Res. Lett., 38, https://doi.org/10.1029/2011GL047968, 2011.
- Hervig, M. E., Gordley, L. L., Stevens, M. H., Russell III, J. M., Bailey, S. M., and Baumgarten, G.: Interpretation of SOFIE PMC measurements: Cloud identification and derivation of mass density, particle shape, and particle size, J. Atmos. Sol.-Terr. Phy., 71, 316-330, https://doi.org/10.1016/j.jastp.2008.07.009, 2009.
 - Hervig, M. E., Siskind, D. E., Bailey, S. M., Merkel, A. W., DeLand, M. T., and Russell III, J. M.: The Missing Solar Cycle Response of the Polar Summer Mesosphere, Geophys. Res. Lett., 46, 10132-10139, https://doi.org/10.1029/2019GL083485, 2019.
 - Hervig, M. E., Siskind, D. E., Bailey, S. M., and Russell III, J. M.: The influence of PMCs on water vapor and drivers behind PMC variability from SOFIE observations, J. Atmos. Sol.-Terr. Phy., 132, 124-134, https://doi.org/10.1016/j.jastp.2015.07.010, 2015.
- Huang, F. T., Mayr, H. G., Russell Iii, J. M., and Mlynczak, M. G.: Ozone and temperature decadal trends in the stratosphere, mesosphere and lower thermosphere, based on measurements from SABER on TIMED, Ann. Geophys., 32, 935-949, https://doi.org/10.5194/angeo-32-935-2014, 2014.
 - Huang, F. T., Mayr, H. G., Russell Iii, J. M., Mlynczak, M. G., and Reber, C. A.: Ozone diurnal variations and mean profiles in the mesosphere, lower thermosphere, and stratosphere, based on measurements from SABER on TIMED, J. Geophys. Res.-Space, 113, https://doi.org/10.1029/2007JA012739, 2008.
- 390 Hultgren, K., and Gumbel, J.: Tomographic and spectral views on the lifecycle of polar mesospheric clouds from Odin/OSIRIS, J. Geophys. Res.-Atmos., 119, 14,129-114,143, https://doi.org/10.1002/2014JD022435, 2014.
 - Jia, J., Murberg, L. E., Løvset, T., Orsolini, Y. J., Espy, P. J., Zeller, L. C. G., Salinas, C. C. J. H., Lee, J. N., Wu, D., and Zhang, J.: Energetic particle precipitation influences global secondary ozone distribution, Communications Earth & Environment, 5, 270, https://doi.org/10.1038/s43247-024-01419-2, 2024.

- Jiang, Y. B., et al.: Validation of Aura Microwave Limb Sounder Ozone by ozonesonde and lidar measurements, J. Geophys. Res.-Atmos., 112, https://doi.org/10.1029/2007JD008776, 2007.
 - Kalicinsky, C., Peters, D. H. W., Entzian, G., Knieling, P., and Matthias, V.: Observational evidence for a quasi-bidecadal oscillation in the summer mesopause region over Western Europe, J. Atmos. Sol.-Terr. Phy., 178, 7-16, https://doi.org/10.1016/j.jastp.2018.05.008, 2018.
- 400 Karlsson, B., and Kuilman, M.: On How the Middle Atmospheric Residual Circulation Responds to the Solar Cycle Close to the Solstices, Journal of Climate, 31, 401-421, https://doi.org/10.1175/JCLI-D-17-0202.1, 2018.
 - Kulikov, M. Y., Belikovich, M. V., Grygalashvyly, M., Sonnemann, G. R., Ermakova, T. S., Nechaev, A. A., and Feigin, A. M.: Nighttime Ozone Chemical Equilibrium in the Mesopause Region, J. Geophys. Res.-Atmos., 123, 3228-3242, https://doi.org/10.1002/2017JD026717, 2018.
- 405 Laštovička, J.: A review of recent progress in trends in the upper atmosphere, J. Atmos. Sol.-Terr. Phy., 163, 2-13, https://doi.org/10.1016/j.jastp.2017.03.009, 2017.
 - Lee, J., Kwak, Y.-S., Kam, H., Kil, H., Park, J., Kim, J., Yang, T.-Y., and Lee, C.: Vertical Wind Profiles in the Mesosphere and Lower Thermosphere Driven by Meteor Radar and Ionospheric Connection Explorer Observations Over the Korean Peninsula, Geophys. Res. Lett., 51, e2023GL106450, https://doi.org/10.1029/2023GL106450, 2024.
- Lee, J. N., and Wu, D. L.: Solar Cycle Modulation of Nighttime Ozone Near the Mesopause as Observed by MLS, Earth and Space Science, 7, e2019EA001063, https://doi.org/10.1029/2019EA001063, 2020.
 - Liu, X., Xu, J., Yue, J., Liu, Y., and Andrioli, V. F.: Trends in the high-latitude mesosphere temperature and mesopause revealed by SABER, Atmos. Chem. Phys., 24, 10143-10157, https://doi.org/10.5194/acp-24-10143-2024, 2024.
- Liu, X., Yue, J., Xu, J., Yuan, W., Russell III, J. M., and Hervig, M. E.: Five-day waves in polar stratosphere and mesosphere temperature and mesospheric ice water measured by SOFIE/AIM, J. Geophys. Res.-Atmos., 120, 3872-3887, https://doi.org/10.1002/2015JD023119, 2015.
 - Lossow, S., Urban, J., Schmidt, H., Marsh, D. R., Gumbel, J., Eriksson, P., and Murtagh, D.: Wintertime water vapor in the polar upper mesosphere and lower thermosphere: First satellite observations by Odin submillimeter radiometer, J. Geophys. Res.-Atmos., 114, https://doi.org/10.1029/2008JD011462, 2009.
- Lübken, F.-J., Berger, U., and Baumgarten, G.: Temperature trends in the midlatitude summer mesosphere, J. Geophys. Res.-Atmos., 118, 13,347-313,360, https://doi.org/10.1002/2013JD020576, 2013.

- Lübken, F.-J., Berger, U., and Baumgarten, G.: On the Anthropogenic Impact on Long-Term Evolution of Noctilucent Clouds, Geophys. Res. Lett., 45, 6681-6689, https://doi.org/10.1029/2018GL077719, 2018.
- Lübken, F. J., Berger, U., and Baumgarten, G.: Stratospheric and solar cycle effects on long-term variability of mesospheric ice clouds, J. Geophys. Res.-Atmos., 114, https://doi.org/10.1029/2009JD012377, 2009.
- Mlynczak, M. G., Hunt, L. A., Marshall, B. T., Mertens, C. J., Marsh, D. R., Smith, A. K., Russell, J. M., Siskind, D. E., and Gordley, L. L.: Atomic hydrogen in the mesopause region derived from SABER: Algorithm theoretical basis, measurement uncertainty, and results, J. Geophys. Res.-Atmos., 119, 3516-3526, https://doi.org/10.1002/2013JD021263, 2014.
- 430 Mlynczak, M. G., et al.: Atomic oxygen in the mesosphere and lower thermosphere derived from SABER: Algorithm theoretical basis and measurement uncertainty, J. Geophys. Res.-Atmos., 118, 5724-5735, https://doi.org/10.1002/jgrd.50401, 2013.
 - Mlynczak, M. G., Hunt, L. A., Russell Iii, J. M., and Marshall, B. T.: Updated SABER Night Atomic Oxygen and Implications for SABER Ozone and Atomic Hydrogen, Geophys. Res. Lett., 45, 5735-5741, https://doi.org/10.1029/2018GL077377, 2018.
 - Mlynczak, M. G., Marshall, B. T., Martin-Torres, F. J., Russell Iii, J. M., Thompson, R. E., Remsberg, E. E., and Gordley, L. L.: Sounding of the Atmosphere using Broadband Emission Radiometry observations of daytime mesospheric O2(1Δ) 1.27 μm emission and derivation of ozone, atomic oxygen, and solar and chemical energy deposition rates, J. Geophys. Res.-Atmos., 112, https://doi.org/10.1029/2006JD008355, 2007.
- Mlynczak, M. G., and Solomon, S.: A detailed evaluation of the heating efficiency in the middle atmosphere, J. Geophys. Res.-Atmos., 98, 10517-10541, https://doi.org/10.1029/93JD00315, 1993.

- Offermann, D., Kalicinsky, C., Koppmann, R., and Wintel, J.: Very long-period oscillations in the atmosphere (0–110 km), Atmos. Chem. Phys., 21, 1593-1611, https://doi.org/10.5194/acp-21-1593-2021, 2021.
- Plane, J. M. C., Gumbel, J., Kalogerakis, K. S., Marsh, D. R., and von Savigny, C.: Opinion: Recent developments and future directions in studying the mesosphere and lower thermosphere, Atmos. Chem. Phys., 23, 13255-13282, https://doi.org/10.5194/acp-23-13255-2023, 2023.
 - Qian, L., Jacobi, C., and McInerney, J.: Trends and Solar Irradiance Effects in the Mesosphere, J. Geophys. Res.-Space, 124, 1343-1360, https://doi.org/10.1029/2018JA026367, 2019.
- Ramesh, K., Mitchell, N. J., Hindley, N. P., and Moffat-Griffin, T.: Long-Term Variability and Tendencies in Mesosphere and Lower Thermosphere Winds From Meteor Radar Observations Over Esrange (67.9°N, 21.1°E), J. Geophys. Res.-Atmos., 129, e2023JD040404, https://doi.org/10.1029/2023JD040404, 2024.
 - Ramesh, K., Sridharan, S., and Vijaya Bhaskara Rao, S.: Influence of solar cycle and chemistry on tropical (10°N–15°N) mesopause variabilities, J. Geophys. Res.-Space, 120, 4038-4051, https://doi.org/10.1002/2014JA020930, 2015.
 - Rapp, M., and Thomas, G. E.: Modeling the microphysics of mesospheric ice particles: Assessment of current capabilities and basic sensitivities, J. Atmos. Sol.-Terr. Phy., 68, 715-744, https://doi.org/10.1016/j.jastp.2005.10.015, 2006.

465

- Remsberg, E., Damadeo, R., Natarajan, M., and Bhatt, P.: Observed Responses of Mesospheric Water Vapor to Solar Cycle and Dynamical Forcings, J. Geophys. Res.-Atmos., 123, 3830-3843, https://doi.org/10.1002/2017JD028029, 2018.
- Remsberg, E. E., et al.: Assessment of the quality of the Version 1.07 temperature-versus-pressure profiles of the middle atmosphere from TIMED/SABER, J. Geophys. Res.-Atmos., 113, https://doi.org/10.1029/2008JD010013, 2008.
- Roble, R. G., and Dickinson, R. E.: How will changes in carbon dioxide and methane modify the mean structure of the mesosphere and thermosphere?, Geophys. Res. Lett., 16, 1441-1444, https://doi.org/10.1029/GL016i012p01441, 1989.
 - Rong, P. P., Russell Iii, J. M., Mlynczak, M. G., Remsberg, E. E., Marshall, B. T., Gordley, L. L., and López-Puertas, M.: Validation of Thermosphere Ionosphere Mesosphere Energetics and Dynamics/Sounding of the Atmosphere using Broadband Emission Radiometry (TIMED/SABER) v1.07 ozone at 9.6 μm in altitude range 15–70 km, J. Geophys. Res.-Atmos., 114, https://doi.org/10.1029/2008JD010073, 2009.
 - Russell III, J. M., et al.: The Aeronomy of Ice in the Mesosphere (AIM) mission: Overview and early science results, J. Atmos. Sol.-Terr. Phy., 71, 289-299, https://doi.org/10.1016/j.jastp.2008.08.011, 2009.
 - Russell, J., Mlynczak, M., Gordley, L., Tansock, J., and Esplin, R.: Overview of the SABER experiment and preliminary calibration results, SPIE Proceedings, 3756, 277-288, https://doi.org/10.1117/12.366382, 1999.
 - Shi, G., Krochin, W., Sauvageat, E., and Stober, G.: Ozone and water vapor variability in the polar middle atmosphere observed with ground-based microwave radiometers, Atmos. Chem. Phys., 23, 9137-9159, https://doi.org/10.5194/acp-23-9137-2023, 2023.
- Siskind, D. E., Marsh, D. R., Mlynczak, M. G., Martin-Torres, F. J., and Russell Iii, J. M.: Decreases in atomic hydrogen over the summer pole: Evidence for dehydration from polar mesospheric clouds?, Geophys. Res. Lett., 35, https://doi.org/10.1029/2008GL033742, 2008.
 - Siskind, D. E., Merkel, A., Marsh, D., Randall, C., Hervig, M., Mlynczak, M., and Russell III, J. J. J. o. G. R. A.: Understanding the effects of polar mesospheric clouds on the environment of the upper mesosphere and lower thermosphere, J. Geophys. Res.-Atmos., 123, 11,705-711,719, https://doi.org/10.1029/2018JD028830, 2018.
- 480 Siskind, D. E., and Stevens, M. H.: A radiative feedback from an interactive polar mesospheric cloud parameterization in a two dimensional model, Adv. Space Res., 38, 2383-2387, https://doi.org/10.1016/j.asr.2005.03.094, 2006.
 - Smith, A. K., Espy, P. J., López-Puertas, M., and Tweedy, O. V.: Spatial and Temporal Structure of the Tertiary Ozone Maximum in the Polar Winter Mesosphere, J. Geophys. Res.-Atmos., 123, 4373-4389, https://doi.org/10.1029/2017JD028030, 2018.
- Smith, A. K., Garcia, R. R., Marsh, D. R., Kinnison, D. E., and Richter, J. H.: Simulations of the response of mesospheric circulation and temperature to the Antarctic ozone hole, Geophys. Res. Lett., 37, https://doi.org/10.1029/2010GL045255, 2010a.
 - Smith, A. K., Garcia, R. R., Marsh, D. R., and Richter, J. H.: WACCM simulations of the mean circulation and trace species transport in the winter mesosphere, J. Geophys. Res.-Atmos., 116, https://doi.org/10.1029/2011JD016083, 2011.

- 490 Smith, A. K., et al.: Satellite observations of ozone in the upper mesosphere, J. Geophys. Res.-Atmos., 118, 5803-5821, https://doi.org/10.1002/jgrd.50445, 2013.
 - Smith, A. K., and Marsh, D. R.: Processes that account for the ozone maximum at the mesopause, J. Geophys. Res.-Atmos., 110, https://doi.org/10.1029/2005JD006298, 2005.
- Smith, A. K., Marsh, D. R., Mlynczak, M. G., and Mast, J. C.: Temporal variations of atomic oxygen in the upper mesosphere from SABER, J. Geophys. Res.-Atmos., 115, https://doi.org/10.1029/2009JD013434, 2010b.
 - Solomon, S. C., Liu, H.-L., Marsh, D. R., McInerney, J. M., Qian, L., and Vitt, F. M.: Whole Atmosphere Simulation of Anthropogenic Climate Change, Geophys. Res. Lett., 45, 1567-1576, https://doi.org/10.1002/2017GL076950, 2018.
 - Vellalassery, A., Baumgarten, G., Grygalashvyly, M., and Lübken, F. J.: Greenhouse gas effects on the solar cycle response of water vapour and noctilucent clouds, Ann. Geophys., 41, 289-300, https://doi.org/10.5194/angeo-41-289-2023, 2023.
 - Venkateswara Rao, N., Espy, P. J., Hibbins, R. E., Fritts, D. C., and Kavanagh, A. J.: Observational evidence of the influence of Antarctic stratospheric ozone variability on middle atmosphere dynamics, Geophys. Res. Lett., 42, 7853-7859, https://doi.org/10.1002/2015GL065432, 2015.
- Vincent, R. A., Kovalam, S., Murphy, D. J., Reid, I. M., and Younger, J. P.: Trends and Variability in Vertical Winds in the Southern Hemisphere Summer Polar Mesosphere and Lower Thermosphere, J. Geophys. Res.-Atmos., 124, 11070-11085, https://doi.org/10.1029/2019JD030735, 2019.

- von Zahn, U., and Berger, U.: Persistent ice cloud in the midsummer upper mesosphere at high latitudes: Three-dimensional modeling and cloud interactions with ambient water vapor, J. Geophys. Res.-Atmos., 108, https://doi.org/10.1029/2002JD002409, 2003.
- Zhang, L., Liu, Z., and Tinsley, B.: Altitude-Dependent Formation of Polar Mesospheric Clouds: Charged Nucleation and In Situ Ice Growth on Zonal and Daily Scales, EGUsphere, 2025, 1-29, https://doi.org/10.5194/egusphere-2025-2330, 2025a.
 - Zhang, L., Liu, Z., and Tinsley, B.: Height-Latitude Patterns of Interannual Climate Variability in the Upper Mesosphere and Lower Thermosphere During Spring and Autumn Months, Geophys. Res. Lett., 52, e2025GL116281, https://doi.org/10.1029/2025GL116281, 2025b.
 - Zhang, W., Chen, G., Zhang, S., Gong, W., Chen, F., He, Z., Huang, K., Wang, Z., and Li, Y.: Statistical Study of the Midlatitude Mesospheric Vertical Winds Observed by the Wuhan and Beijing MST Radars in China, J. Geophys. Res.-Atmos., 125, e2020JD032776, https://doi.org/10.1029/2020JD032776, e2020.